Front. Chem. Sci. Eng. 2022, 16(12): 1761−1771
https://doi.org/10.1007/s11705-022-2195-6

RESEARCH ARTICLE

Co anchored on porphyrinic triazine-based frameworks with excellent biocompatibility for conversion of CO_2 in H_2-mediated microbial electrosynthesis

Folin Liu[1], Shaohua Feng[1], Siyuan Xiu[1], Bin Yang[1,2], Yang Hou[1,2], Lecheng Lei[1,2], Zhongjian Li (✉)[1,2,3]

1 College of Chemical and Biological Engineering, Key Laboratory of Biomass Chemical Engineering of Ministry of Education, Zhejiang University, Hangzhou 310027, China
2 Institute of Zhejiang University—Quzhou, Quzhou 324000, China
3 Academy of Ecological Civilization, Zhejiang University, Hangzhou 310027, China

Abstract Microbial electrosynthesis is a promising alternative to directly convert CO_2 into long-chain compounds by coupling inorganic electrocatalysis with biosynthetic systems. However, problems arose that the conventional electrocatalysts for hydrogen evolution may produce extensive by-products of reactive oxygen species and cause severe metal leaching, both of which induce strong toxicity toward microorganisms. Moreover, poor stability of electrocatalysts cannot be qualified for long-term operation. These problems may result in poor biocompatibility between electrocatalysts and microorganisms. To solve the bottleneck problem, Co anchored on porphyrinic triazine-based frameworks was synthesized as the electrocatalyst for hydrogen evolution and further coupled with *Cupriavidus necator* H16. It showed high selectivity for a four-electron pathway of oxygen reduction reaction and low production of reactive oxygen species, owing to the synergistic effect of Co–N_x modulating the charge distribution and adsorption energy of intermediates. Additionally, low metal leaching and excellent stability were observed, which may be attributed to low content of Co and the stabilizing effect of metalloporphyrins. Hence, the electrocatalyst exhibited excellent biocompatibility. Finally, the microbial electrosynthesis system equipped with the electrocatalyst successfully converted CO_2 to poly-*β*-hydroxybutyrate. This work drew up a novel strategy for enhancing the biocompatibility of electrocatalysts in microbial electrosynthesis system.

Keywords microbial electrosynthesis, hydrogen evolution reaction, metalloporphyrins, biocompatibility, CO_2 conversion

Received April 20, 2022; accepted May 19, 2022

E-mail: zdlizj@zju.edu.cn

1 Introduction

With an extensive consumption of fossil fuels, the concentration of CO_2 in the atmosphere has risen rapidly, which leads to a series of global climate anomalies [1,2] due to the greenhouse effect. To address these crises, plenty of techniques for carbon capture, utilization and storage [3,4] have been developed. Microbial electrosynthesis (MES) stands out owing to its ability to convert CO_2 into long-chain compounds with high added value for one-step operation [5,6] whilst achieving decarbonization ultimately.

MES is a kind of hybrid catalytic system coupling inorganic electrocatalysis with biocatalytic conversion. Specifically, electron mediators such as H_2 [7] and formate [8] are *in-situ* provided by the inorganic electrocatalysis using electricity [9] or solar energy [10]. Electron mediators will be utilized by the microorganisms as reducing equivalents to fix CO_2 into long-chain compounds through diverse metabolic pathways without complicated intermediate processes [11]. H_2-mediated MES system coupling the hydrogen evolution reaction (HER) with H_2-oxidizing autotroph bacteria is widely studied and considered as one of the most efficient systems [12–14]. Nevertheless, the biocompatibility between electrocatalysts and bacteria is the bottleneck problem of MES systems [6,15]. On one hand, producing reactive oxygen species (ROS) such as superoxide ($\cdot O_2^-$), hydrogen peroxide (H_2O_2) and hydroxyl radical ($\cdot$OH), is thermodynamically favored under the potential of HER in neutral solution [16]. In other words, the by-production of ROS is inevitable for electrocatalysts when operating. ROS are evident to inflict irreversible damage to DNA and phospholipid bilayer, when the oxidative stress exceeds the capacity of the endogenous antioxidant defense

system [17,18]. On the other hand, owing to the existence of the dynamic equilibrium between metallic dissolution and precipitation on the phase interface of electrocatalysts [19], metal elements tend to dissolve into electrolytes despite a negative potential is applied on electrocatalysts. It is reported that a trace of metal ions (approximately part per million level) leaching from electrocatalysts is capable of inhibiting bacterial growth [12]. Because metal ions in the electrolyte (i.e., culture medium) can form complex bonds with proteins which may result in misfold and inactivation of the enzymes necessary for microbial metabolism [20]. Additionally, it is commonly required for MES system to continuously operate for a long time (two weeks) [21]. Hereby, it puts forward extreme demand for electrocatalysts on electrochemical stability.

Recently, covalent triazine frameworks (CTF) have attracted great attention owing to abundant nitrogen sites, hierarchically porous architectures and high chemical stability [22,23]. Moreover, metal elements can be anchored on porphyrin architectures in CTF forming metal coordinated nitrogen ($M–N_x$) sites, which are reactive for varieties of electrochemical reactions with excellent stability. Anchoring metal on CTF as the electrocatalyst for HER would be an ideal strategy to debottleneck the poor biocompatibility between electrocatalysts and bacteria for the following reasons. Firstly, these catalysts have been reported to exhibit a highly efficient four-electron oxygen reduction reaction (ORR) pathway in both acid and alkaline media [24–26], which may be attributed to the synergistic effect between $M–N_x$ [22]. Therefore, partial reduction of oxygen will not be the dominant pathway and by-production of ROS will be greatly eliminated. Secondly, metal elements exist in the form of metalloporphyrins. Due to the strong covalent metal-support interaction, metal elements can be fixed in porphyrin motifs with excellent stability [27]. Concerning limited porphyrin motifs in CTF, the metal loading of catalysts is extremely low, perhaps less than 1 wt % [28]. Accordingly, the concentration of metal ions dissolved from catalysts will be prominently decreased on account of the stabilizing effect of metalloporphyrins and low content of metal elements. In addition, anchoring metal elements on CTF is a potential method for preparation of single-atom catalysts in view of highly distributed porphyrin motifs and incorporated metalloporphyrin architectures [29]. It can bridge the gap between heterogeneous and homogeneous catalysis, thus maximizing the catalytic efficiency of reactive sites and achieving high catalytic performance [30]. Above all, anchoring metal on CTF is a promising strategy to enhance the HER performances and biocompatibility of electrocatalysts for MES system.

Herein, in this study, 3d transition metal elements, including Fe, Co, Ni and Cu were selected as the candidates owing to their merits of decent HER activity and relatively low cost. Fe, Co, Ni and Cu anchored on porphyrinic triazine-based frameworks (M@PTF) were synthesized as the electrocatalysts for HER in MES system. Linear sweep voltammetry (LSV) and Tafel slope was employed to select the best HER electrocatalysts among M@PTF. Transmission electron microscopy-energy dispersive spectrometer (TEM-EDS), X-ray diffraction (XRD), Fourier transform infrared spectroscopy (FTIR), Raman, Brunauer–Emmett–Teller (BET) and X-ray photoelectron spectroscopy (XPS) were implemented to make insights into the physical properties. Moreover, the concentration of ROS, including $\cdot O_2^-$, H_2O_2 and ·OH, were determined (semi-) quantitatively using corresponding probes. Whilst stainless steel (SS) was selected as the comparison. Furthermore, the biocompatibilities of electrocatalysts were evaluated by growth curves in MES system and spot assays. The concentrations of metal leaching were monitored throughout the operation. Finally, MES systems were operated equipped with synthesized electrocatalysts, coupling with a H_2-oxidizing bacterium, *Cupriavidus necator* H16 [31] for CO_2 conversion to high value-added bioplastic, poly-*β*-hydroxybutyrate (PHB).

2 Experimental

2.1 Synthesis of M@PTF

The preparation of the M@PTF (M = Fe, Co, Ni, Cu) was previously reported with a slight modification [28]. 5.65 g of 4-cyanobenzaldehyde and 3 mL of pyrrole were added into a flask containing 100 mL of propionic acid. The mixture was heated to 145 °C for 12 h under reflux with vigorous stirring. The insoluble substance was washed three times with methanol, ethyl acetate and tetrahydrofuran in turn. The precursor was obtained after drying at 60 °C for 24 h and labeled as TP. In order to anchor 3d transition metal elements on TP, 0.715 g of TP and 12.8 mmol of $M–Cl_2$ were suspended with 100 mL of *N*,*N*-dimethylformamide, and the mixture was heated to 160 °C for 10 h under reflux with vigorous stirring. The residue was washed three times with 1.0 $mol·L^{-1}$ HCl and deionized water, then dried at 60 °C for 24 h. The obtained product was donated as M@TP. In the last procedure of synthesis, 0.3 mmol of M@TP and 10 mol of $ZnCl_2$ were added into a quartz ampule. The ampule was evacuated and sealed before calcining. It was heated to 600 °C for 40 h at a heating rate of 5 $°C·min^{-1}$. Finally, the product was washed with deionized water followed by 1.0 $mol·L^{-1}$ HCl. After filtration and drying, the black powder was taken as the target product of M@PTF.

2.2 Characterization

2.2.1 Physical characterizations

The morphology and structural properties of Co@PTF

was observed by TEM (Hitachi HT-7700). TEM was equipped with an EDS (Oxford X-max 80) to define the element distribution. The inductively coupled plasma optical emission spectroscopy (ICP-MS, PerkinElmer NexION 300X) was employed to quantify the content of metal elements. The crystal structure pattern was recorded by XRD (Bruker D8 Advance). FTIR (Thermo Fisher Scientific Nicolet iS10) was used for functional group measurement. Raman spectrum was obtained by a Raman spectrometer (LabRam HR Evolution). The specific surface area was analyzed by TriStar II Plus (N_2, –196 °C) and the pore size distribution was calculated by the heterogeneous surface nonlocal density functional theory (NLDFT) model. The XPS (Thermo Fisher Scientific K-Alpha) was implemented to determine the composition and atomic valence state.

2.2.2 Electrochemical characterizations

The preparation of electrodes and fabrication of three-electrode test system was manifested in Electronic Supplementary Material (ESM). The LSV was performed with the potential range from –1.5 to –0.4 V (all the potentials were applied versus saturated Ag/AgCl in the Experimental section) at a scan rate of 5 $mV \cdot s^{-1}$, after at least 20 cycles of cyclic voltammogram to eliminate the influence of impurities on the electrode surface. The rotating ring-disk electrode (RRDE) measurements were carried with a glassy carbon ring-disk electrode (4 mm diameter) with a Pt ring-disk electrode as the working electrode and MM as the electrolyte. High-purity O_2 was utilized to provide the O_2-saturated solution before tests. LSV tests for ORR were conducted at a rate of 5 $mV \cdot s^{-1}$ with the potential range from –0.6 to 0.6 V. The ring potential was constant at 0.5 V. The hydrogen peroxide yield (H_2O_2%) and the electron transfer number (n) were calculated with the following equations:

$$H_2O_2\% = \frac{\frac{I_r}{N}}{I_d + \frac{I_r}{N}} \times 200, \quad (1)$$

$$n = \frac{I_d}{I_d + \frac{I_r}{N}} \times 4, \quad (2)$$

where I_r was the ring current, I_d was the disk current and N was current collection efficiency of the Pt ring. N was calibrated by measuring the ratio of ring current densities and disk current densities under the same parameters mentioned above except the electrolyte containing 10 $mmol \cdot L^{-1}$ $K_3Fe(CN)_6$ and 100 $mmol \cdot L^{-1}$ KCl [32]. N was defined as average value to be 0.497 (Fig. S1, cf. ESM).

2.3 Determination of ROS

Semi-quantitation of the concentration of $\cdot O_2^-$ was measured by the $\cdot O_2^-$ specific probe hydroethidine (HE) [33]. HE can be oxidized by $\cdot O_2^-$ to produce fluorescent ethidium, which emitted fluorescence (λ_{ex} = 470 nm, λ_{em} = 610 nm).

The accurate concentration of H_2O_2 was measured using a fluorimetric hydrogen peroxide assay kit (Sigma-Aldrich) by monitoring the red fluorescent reaction product (λ_{ex} = 540 nm, λ_{em} = 590 nm) with a fluorescent microplate reader (Tecan Infinite 200 Pro) [12]. Calibration curves in Experimental section were shown in Fig. S2 (cf. ESM). The concentration of H_2O_2 was quantified by comparing it with a calibration curve obtained from H_2O_2 standards ranging from 0 to 10 $\mu mol \cdot L^{-1}$ (Fig. S2(a)).

The concentration of ·OH was determined using the terephthalic acid (TA) method [34]. TA was added into the electrolyte as the probe then reacted with ·OH producing HO-TA which resulted in the emission of fluorescence (λ_{ex} = 320 nm, λ_{em} = 425 nm). The signal was recorded and translated in terms of concentration via the calibration curve (Fig. S2(b)).

2.4 MES system operation

The MES system was operated in a single-chamber water-splitting reactor (Fig. S3, cf. ESM). The as-prepared carbon paper or SS electrode and Pt mesh (1 × 1 cm^2) were employed as the working electrode and the counter electrode respectively. Details of the preparation for the MES reactor and pre-culture for strain were described in ESM. Before inoculation, the reactor as well as electrolyte was supposed to be sterilized under 121 °C for 20 min. The re-suspended strain was inoculated into 150 mL culture medium through a sampling tube until the optical density at 600 nm (OD_{600}) of the electrolyte ranged from 0.13 to 0.16. Next, the reactor was purged with CO_2 for at least 20 min to ensure saturation of CO_2 in the electrolyte then sealed. The applied current densities were supplied with an electrochemical workstation and the changes of the potential were recorded. 2.5 mL of electrolytes were sampled every day to define OD_{600} using an ultraviolet-visible spectrometer. It was centrifuged at 7000 $r \cdot min^{-1}$ for 7 min then stored at 0 °C before quantification of PHB titers (see details in ESM). The entire electrolyte was purged with CO_2 for 20 min for re-saturation.

2.5 Spot assays

Spot assays of MES systems were performed in the same procedures as MES system without CO_2 aeration. Spot assays for half-maximal inhibitory concentration (IC_{50}) of metal elements were conducted in shaking flasks containing different concentrations of metal elements in MM with similar inoculating concentration. Hence, 100 μL of solution was sampled and diluted 1:10 in MM. Three serial 10-fold dilutions were made and 3 μL of each dilution was spotted on the Luria–Bertani broth agar

plate. Plates were supposed to be grown for 3 d at 30 °C before imaging.

3 Results and discussion

3.1 Electrochemical characterizations

Fabrication procedures and HER performances for M@PTF were illustrated in Fig. 1. As shown in Fig. 1(a), condensation of 4-cyanobenzaldehyde and pyrrole was used to form porphyrin motifs. $FeCl_2$, $CoCl_2$, $NiCl_2$ and $CuCl_2$ were chosen as the candidates for anchoring. Frameworks were fabricated under trimerization reaction using the ionothermal method. The final as-obtained samples were labeled as M@PTF (M = Fe, Co, Ni, Cu).

H_2 produced at the cathode will be utilized by membrane-bound and soluble hydrogenases of *C. necator* to generate the adenosine triphosphate in intracellular energy transfer and reducing equivalents (Nicotinamide adenine dinucleotide phosphate), furtherly driving CO_2-fixing metabolic cycles. Therefore, it is imperative for electrocatalysts to catalyze HER efficiently and supply sufficient H_2 for metabolism.

The HER performances of catalysts were evaluated using a typical three-electrode configuration. The HER performances of as-obtained M@PTF were determined by the LSV method. As depicted in Fig. 1(b), Co@PTF exhibited the lowest overpotential of 575 mV at the current density of –1 mA·cm^{-2}. Furthermore, the Tafel slope (Fig. 1(c)) of Co@PTF was calculated to be 79.9 mV·dec^{-1}, which was the lowest among M@PTF (232.0 mV·dec^{-1} for Fe@PTF, 211.2 mV·dec^{-1} for Ni@PTF and 119.5 mV·dec^{-1} for Cu@PTF, respectively). These results indicated that Co@PTF showed the best catalytic performance of HER among M@PTF. Besides, the Tafel slope of Co@PTF was between 39 and 118 mV·dec^{-1} in neutral media, determining the rate-limiting step to be the Heyrovsky reaction. All of Tafel slopes of Fe@PTF, Ni@PTF and Cu@PTF were calculated to exceed 118 mV·dec^{-1}, indicating the rate-limiting step to be Volmer reaction [35]. Namely, the rapid HER kinetics of Co@PTF may be attributed to the low energy barrier for initial water dissociation ($H_2O + e^- \rightarrow H_{ad} + OH^-$) and moderate surface adsorption of OH^- [36]. Consequently, Co@PTF was chosen as the catalyst for HER in the subsequent experiments.

3.2 Physical characterization

The physical characterization results of Co@PTF were exhibited in Fig. 2. Co@PTF showed the block morphology on the basis of TEM image (Fig. 2(a)). Additionally, the elemental mapping images (Fig. 2(b)) revealed that Co elements were apparently rarer than other elements but homogeneously distributed over the entire structure, implying Co element in an atomically dispersed form. Interestingly, the Co content of Co@PTF was precisely determined to be only 0.86 wt % by ICP-MS. XRD pattern (Fig. 2(c)) exhibited two diffraction

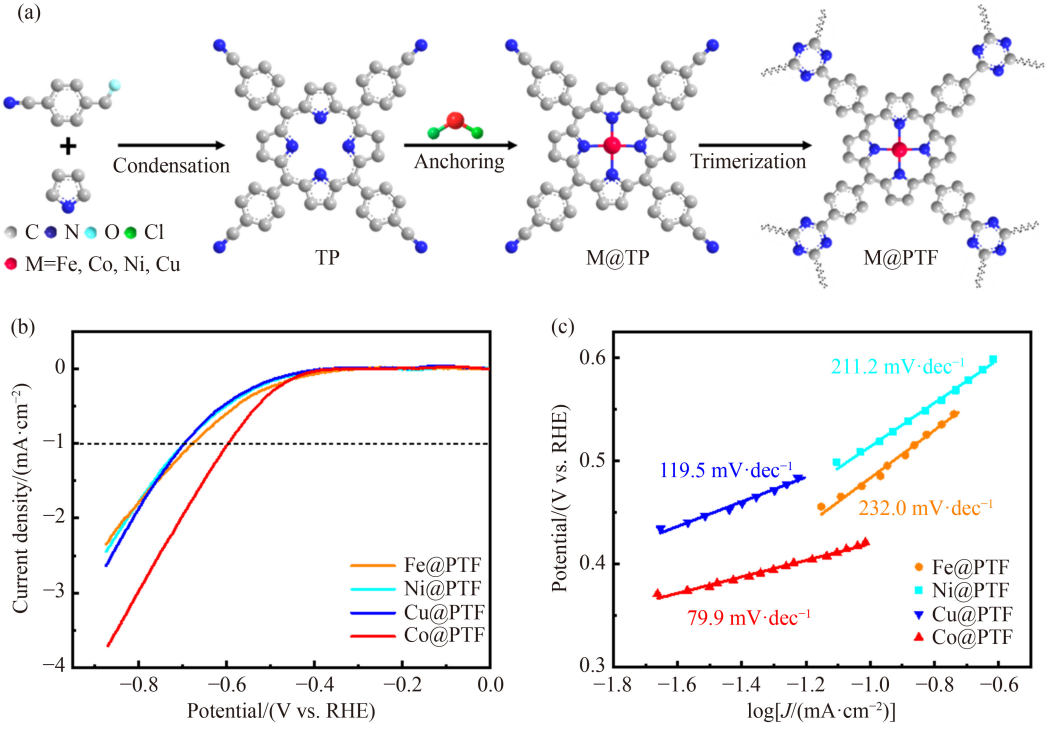

Fig. 1 (a) Schematic illustration of the fabrication procedures for M@PTF; (b) LSV curves; (c) corresponding Tafel slopes of M@PTF (M = Fe, Co, Ni, Cu) in MM without IR correction.

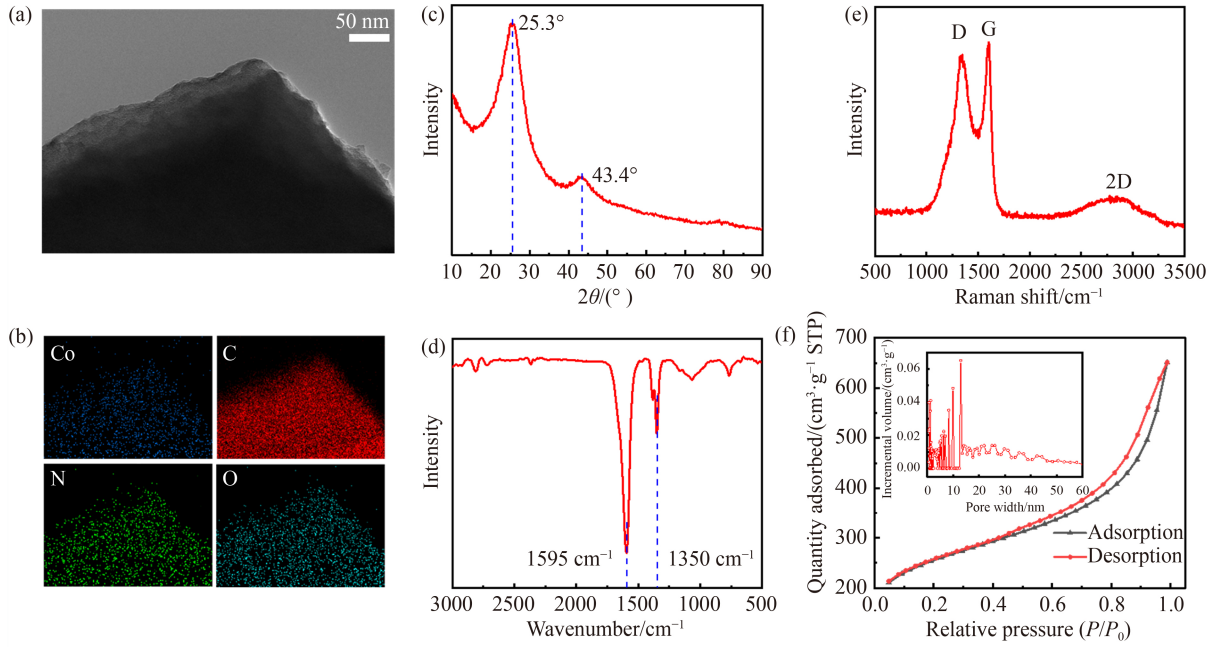

Fig. 2 (a) TEM image and (b) elemental mapping images of Co, C, N, and O, (c) XRD pattern, (d) FTIR spectrum, (e) Raman spectrum, (f) N_2 adsorption–desorption isotherm and pore size distribution (inset) of Co@PTF.

peaks centered at 25.3° and 43.4°, which were ascribed to the (002) face of amorphous graphitic carbon and the (100)/(101) faces of graphitic carbon respectively. No diffraction peak of metal or metal oxides was observed, indicating Co element probably dispersed atomically, which was beneficial for enhancing the utilization efficiency of Co sites. As revealed by FTIR (Fig. 2(d)), the peaks at 1350 and 1595 cm^{-1} were attributed to characteristic vibration peaks of triazine rings, demonstrating the successful trimerization reaction [37]. From Raman spectrum (Fig. 2(e)), there were a sharp D-band at ~1340 cm^{-1} and a sharp G-band at ~1590 cm^{-1} as well as a broad 2D-band at ~2800 cm^{-1}. The ratios of the G-band and D-band intensity were calculated to be 0.95, indicating a partial graphitization. Additionally, a broad 2D-band was discovered, probably attributed to some layered graphene-like architectures. High temperature during ionothermal method may account for the properties of partial graphitization and layered graphene-like architectures, which can enhance the electron transfer capacity, improve conductivity and accelerate electrochemical reaction furtherly [22]. As can be seen from Fig. 2(f), the N_2 adsorption–desorption isotherm of Co@PTF showed hysteresis loops at the relative pressure range from 0.43 to 1.0, which was classified as type IV H3 isotherms, suggesting the formation of irregular micro- and meso-pores. In addition, the BET surface area of the sample was measured to be 867.98 $m^2 \cdot g^{-1}$. The distribution of pore size was calculated to be 0–13.5 nm as well as the average pore size to be 6.91 nm by NLDFT method. The hierarchically porous structure with high special areas can expose more reactive sites, facilitating the mass transfer and maximizing utilization efficiency of reactive sites, thus boosting the catalytic activity for HER [38].

In addition, XPS was carried out to determine the elemental compositions and electronic states (Fig. 3). As exhibited in Fig. 3(a), the XPS survey spectrum confirmed the evident presence of C, N and O elements. The presence of Co element was hardly identified on account of low metal loading. Delicate confirmation for the existence of Co element was gotten via the high-resolution spectrum of Co 2p (Fig. 3(b)). The content of each element was summarized in Table S1 (cf. ESM). More than 5 wt % of N element was detected, which endowed abundant C–N sites possibly catalytic for HER [39] and enhanced the biocompatibility of the surface exposed to microorganisms [40]. The high-resolution spectrum of N 1s (Fig. 3(c)) was deconvoluted into three types of N species, where the peaks located at 398.3, 400.3 and 401.6 eV were corresponding to triazine-N, Co–N and graphitic-N, respectively. The existence of triazine-N confirmed the successful occurrence of trimerization reaction. Co–N was originated from the Co–N_x, whose synergistic effect between Co and N may modulate the charge distribution as well as adsorption energy of intermediates concerning ORR and thereby boost the four-electron pathway of ORR [41]. Partial graphitization while calcining can interpret the presence of graphitic-N. Moreover, the proportions of the three types of N species were fitted to be 42.67% for triazine-N, 31.35% for Co–N and 25.98% for graphitic-N. The triazine-N was the dominant species, which was reported to be beneficial for atomic H_2 adsorption, facilitating the cracking of H_2O molecules [42]. From the high-resolution spectrum of C 1s (Fig. 3(d)), the fitted peak centered at

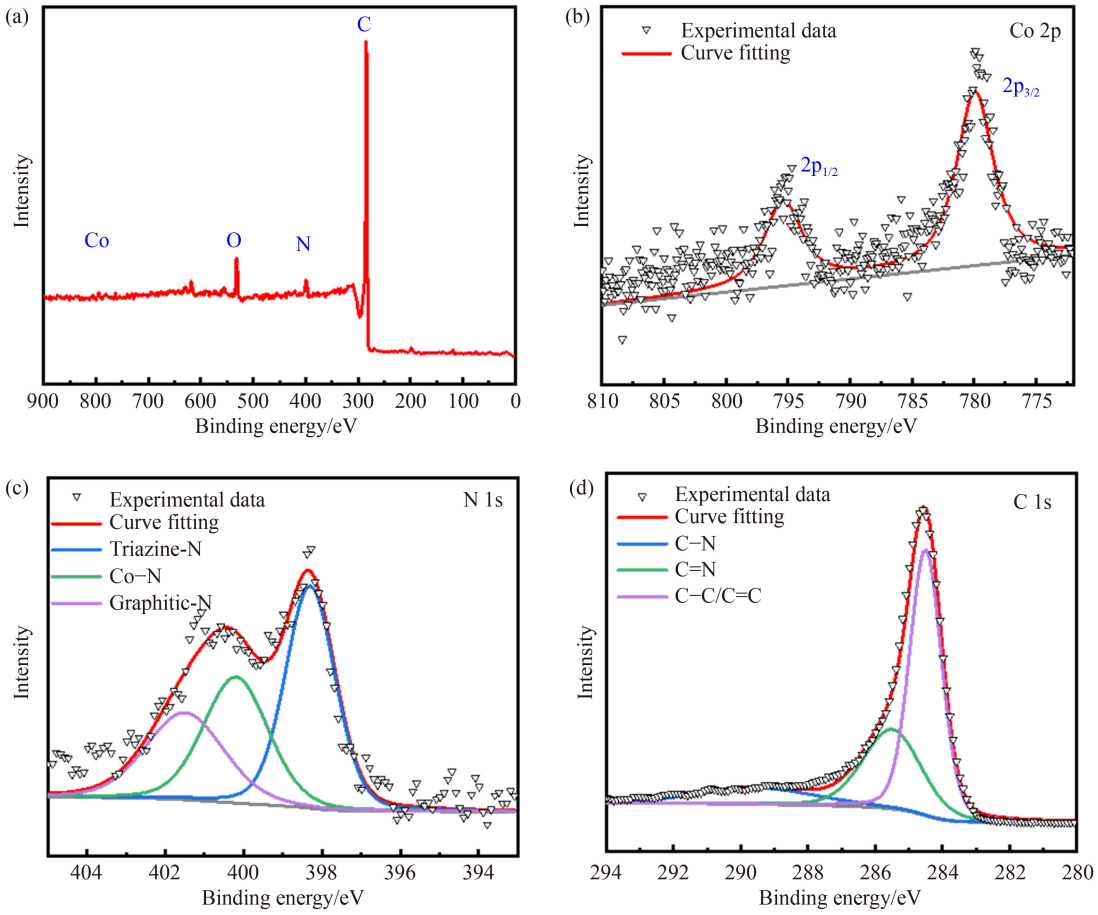

Fig. 3 (a) XPS survey spectrum and high-resolution XPS spectra of (b) Co 2p, (c) N 1s and (d) C 1s of Co@PTF.

285.6 eV was assigned to the C=N bond, which was attributed to trimeric rings in the structure.

3.3 Determination of ROS

O_2 is the electron acceptor of aerobic metabolism and is necessary for *C. necator* to fix CO_2 into PHB [43]. Accordingly, MES system is operated in a single-chamber reactor, where O_2 is continuously produced from the anode then dissolves into electrolytes for microbial assimilation. Inevitably, ROS to which O_2 is partially reduced will be generated at the cathode, because the overpotentials of ROS are lower than that of HER in neutral solution [16]. ROS are highly oxidative intermediates. There are three major species recognized, including $\cdot O_2^-$, H_2O_2 and ·OH [44]. On the basis of the reaction pathway [45] shown in Fig. S4 (cf. ESM), the formation of ROS mainly depends on the two-electron instead of four-electron ORR pathway. H_2O_2 and ·OH are known as nonselective oxidants in the field of advanced oxidation [46], whose oxidative abilities are so strong that organic biomolecules such as DNA, phospholipid bilayer and proteins will be subjected to irreversible damage. Although $\cdot O_2^-$ induces less oxidative stress, it is still worth detecting its concentration since $\cdot O_2^-$ is the precursor of the other ROS [47]. To determine the relative yields of ROS, SS was chosen for comparison. Semi-quantitation of the concentration of $\cdot O_2^-$ was characterized by a $\cdot O_2^-$ specific probe on the base that the intensity showed a positive correlation with the concentration of $\cdot O_2^-$. The determination results of ROS were shown in Fig. 4. The intensity of Co@PTF was lower than that of SS throughout the test exhibited in Fig. 4(a). Accordingly, less production of $\cdot O_2^-$ with Co@PTF than SS can be concluded. As illustrated in Fig. 4(b), the H_2O_2 concentration of Co@PTF got to the maximum value of approximately 42.2 μmol·L^{-1}, which was only one-fifteenth as many as that of SS (611.3 μmol·L^{-1}). The ·OH concentration was determined using the TA method. As can be seen from Fig. 4(c), the ·OH concentration of Co@PTF reached the maximum value of 0.276 μmol·L^{-1} at the sampling time of 5 h. On the contrary, the ·OH concentration of SS got to 5 times larger than that of Co@PTF (1.47 μmol·L^{-1}). The above results proved less production of ROS, including H_2O_2, ·OH, and $\cdot O_2^-$ with Co@PTF than SS.

In order to explore the mechanism of the low production of ROS, the H_2O_2% and n of Co@PTF measured by RRDE were exhibited in Fig. 4(d). The H_2O_2% was calculated to be less than 12% and the n was calculated to be more than 3.75 within the potential window of ORR (ranging from 0.5 to 0.8 V vs. RHE

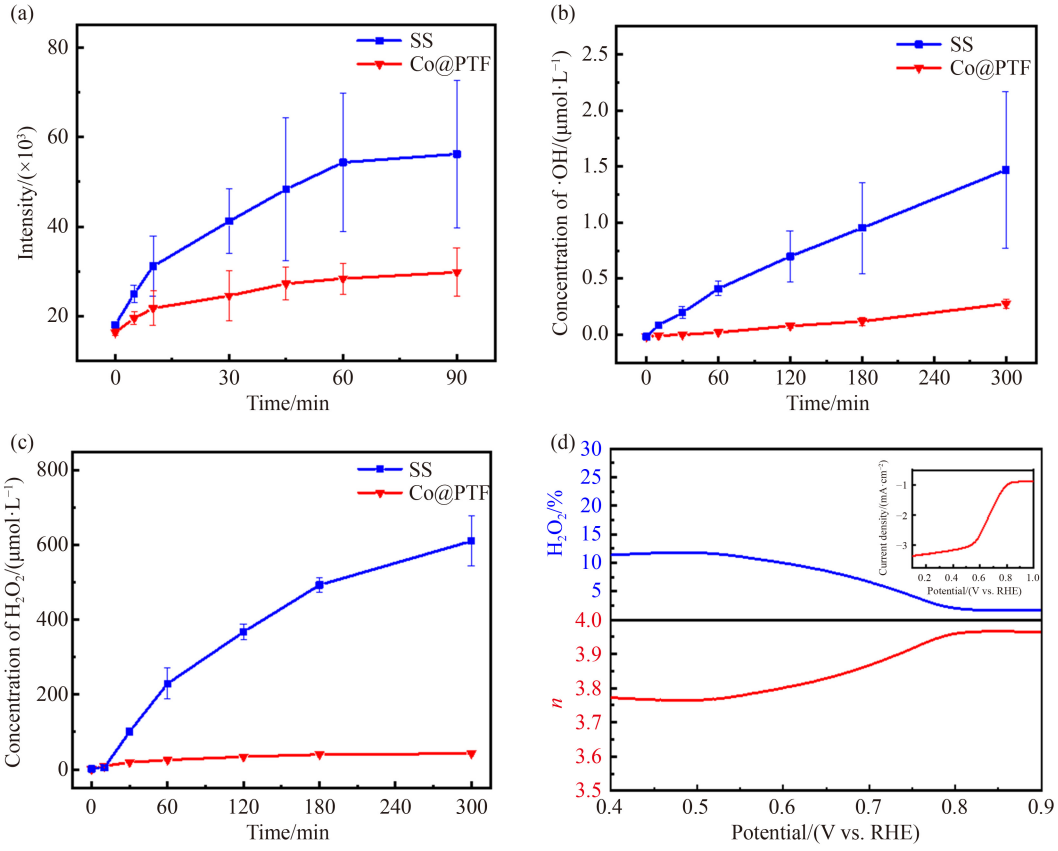

Fig. 4 Concentration of (a) $\cdot O_2^-$, (b) H_2O_2, (c) ·OH of Co@PTF using SS and Co@PTF as cathode at the current density of –1 mA·cm^{-2} (Error bars denote SEM, n = 3). (d) H_2O_2 yield, n and LSV curve for ORR (inset) of Co@PTF obtained from RRDE measurements.

(reversible hydrogen electrode), shown in the inset curve of Fig. 4(d)), which suggested a highly efficient four-electron ORR pathway [48]. Incredible selectivity of the four-electron ORR pathway may be attributed to the synergistic effect of Co–N_x modulating the charge distribution as well as adsorption energy of intermediates concerning ORR [22], which restrains the reduction reaction from O_2 to ROS.

3.4 Evaluation of biocompatibility

Two methods were employed to investigate the biocompatibility of Co@PTF (Fig. 5). Spot assay was employed as the first method under the current density of –1 mA·cm^{-2}. Spot assay is a kind of technique to demonstrate cell viability, where every spot is a single colony proliferated from survived bacteria in the sample. As depicted in Fig. 5(a), Co@PTF exhibited better biocompatibility than SS. Less production of ROS for Co@PTF inflicts *C. necator* relatively weak oxidative stress, which leads to more amounts of bacteria surviving. The growth curves were carried out in the MES systems equipped with Co@PTF and SS as the cathodes under three different current densities (–1, –2 and –4 mA·cm^{-2}).

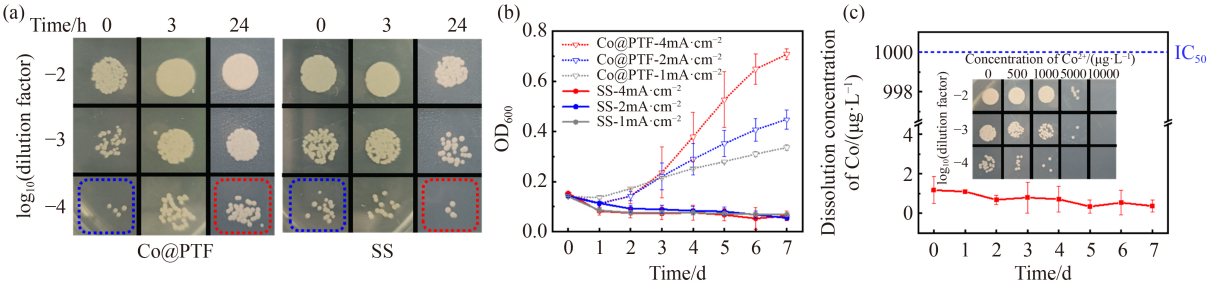

Fig. 5 (a) Spot assays of Co@PTF and SS before starting electrolysis (0 h), after 3 and 24 h of electrolysis at the current density of –1 mA·cm^{-2}. (b) Growth curves of the MES systems equipped with Co@PTF and SS as the cathodes at current densities of –1, –2 and –4 mA·cm^{-2}. (c) Dissolution concentration of Co in the electrolyte of Co@PTF and spot assays of *C. necator* for different concentrations of Co^{2+} (inset). (All the samples of spot assays were grown on plates with different dilution factors. Error bars denote SEM, n = 3).

As displayed in Fig. 5(b), the maximum OD_{600} value of MES systems equipped with Co@PTF at the current densities of –1, –2 and –4 mA·cm^{-2} are 0.335, 0.448 and 0.708, respectively. Higher current densities produce more amount of H_2 and supply more bacteria to grow. As for SS, *C. necator* was unable to grow prosperously and maintained at a poor level of OD_{600} below 0.1 irrespective of current densities. Accordingly, the bacterial growth in MES system equipped with Co@PTF was superior to that of SS. Hence, better biocompatibility of Co@PTF than SS can be concluded.

Additionally, metal leaching from cathodes is regarded as an important factor in biocompatibility, which may form complexes with proteins on the surface of the cell membrane inactivating inherit activity or cross the membranes then exert diverse toxic effects in the cytoplasm. Thus, the dissolution concentration of Co in the electrolyte of the MES system equipped with Co@PTF was monitored. Figure 5(c) showed that the dissolution concentration of Co was found to maintain below 2 μg·L^{-1}, which can be ascribed to the stabilizing effect of metalloporphyrins and low Co loading. It was confirmed by the results of spot assays displayed in Fig. 5(c) (inset) that the IC_{50} of Co was approximately 1000 μg·L^{-1}, which was far beyond the concentration detected. Namely, Co leaching from Co@PTF will not inhibit the growth of *C. necator* throughout the operation. This is another reason why Co@PTF exhibited excellent biocompatibility.

3.5 MES system operation

To evaluate the overall MES performance, Co@PTF and SS were used as cathodes of MES and *C. necator* was inoculated under the current density of –6 mA·cm^{-2}. The specific operating conditions were shown in Fig. 6. As illustrated in Fig. 6(a), the profile of OD_{600} in the MES system equipped with Co@PTF was a typical S shape bacterial growth curve and the maximal OD_{600} value reached 1.54. In contrast, OD_{600} value in the MES system equipped with SS decreased to around 0.075. Similar phenomenon can be discovered in the concentration of biosynthetic PHB shown in Fig. 5(b). The PHB produced in the MES system equipped with Co@PTF started to accumulate when *C. necator* was faced with nutrient constraints after 2 d, showing a good agreement with previous report [12]. From day 2 to day 5, rapid accumulation was obtained and the rate was calculated to be 40.9 mg·L^{-1}·d^{-1}. The maximum concentration of the PHB reached 252.2 mg·L^{-1} on the day 7. As depicted in Fig. 6(c), the maximum proportion of PHB in the MES system equipped with Co@PTF reached up to 31.8% far exceeding that equipped with SS. Besides, energy conversion efficiency (ECE) is a pivotal indicator for energy conversion devices. The calculation details of ECE from electricity to chemical are unfolded in ESM. As can be seen from Fig. 6(d), the ECE curve in the system equipped with Co@PTF presented the trend that increased firstly and then decreased, where the peak value of 4.66% appeared on the day 4. The reason why the

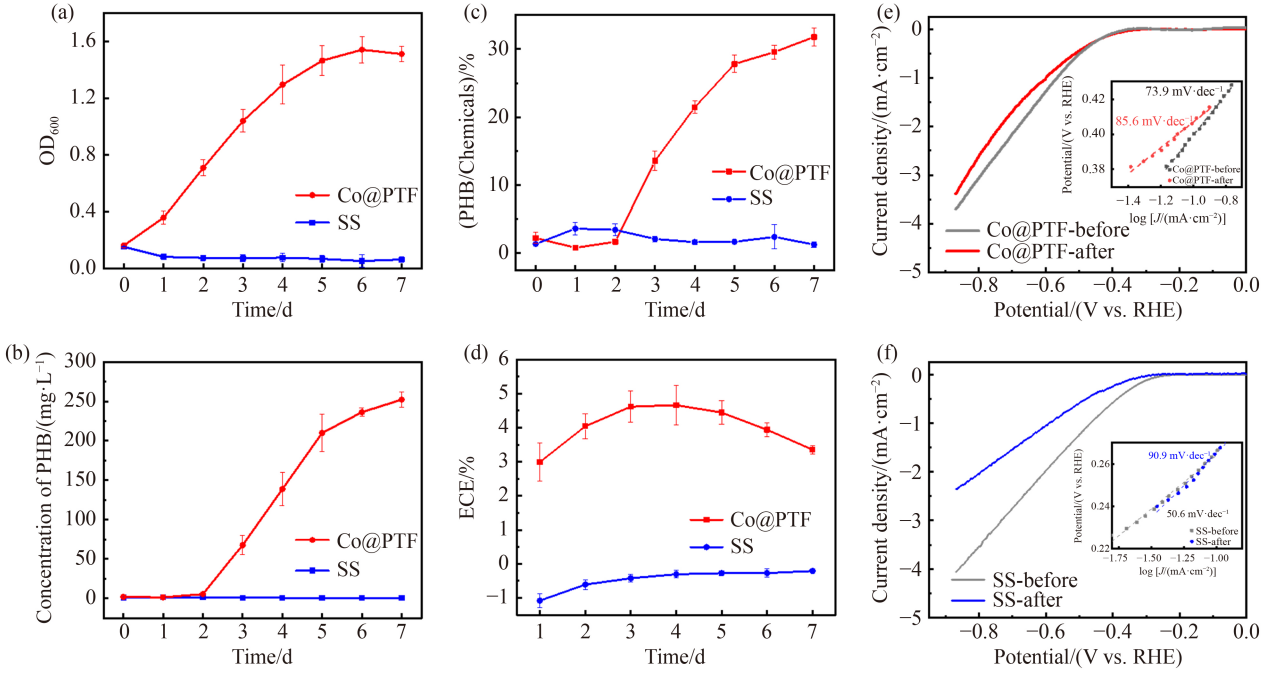

Fig. 6 The profiles of (a) OD_{600} and (b) concentration of PHB. (c) Proportion of PHB in chemicals and (d) ECE during MES systems operation under the current density of –6 mA·cm^{-2} equipped with Co@PTF and SS (Error bars denote SEM, n = 3). (e) LSV curves and Tafel slopes (inset) of Co@PTF before and after MES system operation. (f) LSV curves and Tafel slopes (inset) of SS before and after MES system operation.

maximum value of ECE existed can be clarified as follows. During the rising period, bacterial multiplication made it possible for better use of H_2, which can account for the increase of ECE. The decrease of ECE was owing to the apoptosis of bacteria. With continuing apoptosis of productive bacteria, the utilization of H_2 was insufficient and the impedance of cell reduced gradually, leading to the decrease of ECE and cell potential drop (Fig. S5, cf. ESM). Another issue was the degradation of the catalytic performance for HER, which meant that the applied potential had to increase to achieve the same current density. All values of ECE were negative in the MES system equipped with SS, implying this system failed to convert external electric energy to biosynthetic compounds, which was in accord with the results of OD_{600} and PHB production.

Furthermore, the HER performances of cathodes after 7 d of continuous operation were investigated to evaluate the stability. As exhibited in Figs. 6(e) and 6(f), no obvious decay in the catalytic performance of the Co@PTF was observed while the catalytic performance of SS showed a sharp decrease. Excellent stability of Co@PTF may originate from the stabilizing effect of metalloporphyrins and inherent chemical stability of porphyrinic triazine-based frameworks. Above all, the MES system equipped with Co@PTF successfully converted CO_2 to high value-added product PHB with excellent stability.

4 Conclusions

In summary, metal elements (Fe, Co, Ni and Cu) anchored on porphyrinic triazine-based frameworks were synthesized as the HER electrocatalysts for MES system. Co@PTF showed superior HER activity among M@PTF. Beneficial from the synergistic effect of Co–N_x modulating the charge distribution as well as adsorption energy of intermediates concerning ORR, *n* of Co@PTF was determined to be 3.75. Besides, the by-production of ROS was extremely low owing to its high selectivity for a four-electron pathway of ORR. Moreover, less than 2 $\mu g \cdot L^{-1}$ of Co leaching from Co@PTF was detected and excellent stability of Co@PTF was discovered during 7 d of operation, which can be attributed to low Co loading and the stabilizing effect of metalloporphyrins. Excellent biocompatibility and stability of Co@PTF can be concluded. Furtherly, Co@PTF was coupled with *C. necator* H16 in MES system, successfully converting CO_2 to PHB with excellent stability. This work develops a novel strategy for enhancing the biocompatibility of electrocatalysts for MES. Nevertheless, there are still enormous efforts to be devoted to revealing the mechanism of coupling with inorganic-biological system to enhance the overall ECE for practical application.

Acknowledgements This project was supported by the National Natural Science Foundation of China (Grant Nos. 22122812, 22075245 and 21961160742).

Electronic Supplementary Material Supplementary material is available in the online version of this article at https://dx.doi.org/10.1007/s11705-022-2195-6 and is accessible for authorized users.

References

1. Shindell D, Smith C J. Climate and air-quality benefits of a realistic phase-out of fossil fuels. Nature, 2019, 573(7774): 408–411
2. Peters G P, Andrew R M, Canadell J G, Friedlingstein P, Jackson R B, Korsbakken J I, Le Quéré C, Peregon A. Carbon dioxide emissions continue to grow amidst slowly emerging climate policies. Nature Climate Change, 2020, 10(1): 3–6
3. Rau G H, Willauer H D, Ren Z J. The global potential for converting renewable electricity to negative-CO_2-emissions hydrogen. Nature Climate Change, 2018, 8(7): 621–625
4. Yan Y L, Borhani T N, Subraveti S G, Pai K N, Prasad V, Rajendran A, Nkulikiyinka P, Asibor J O, Zhang Z E, Shao D, Wang L, Zhang W, Yan Y, Ampomah W, You J, Wang M, Anthony E J, Manovic V, Clough P T. Harnessing the power of machine learning for carbon capture, utilisation, and storage (CCUS)—a state-of-the-art review. Energy & Environmental Science, 2021, 14(12): 6122–6157
5. Fang X, Kalathil S, Reisner E. Semi-biological approaches to solar-to-chemical conversion. Chemical Society Reviews, 2020, 49(14): 4926–4952
6. Prévoteau A, Carvajal-Arroyo J M, Ganigué R, Rabaey K. Microbial electrosynthesis from CO_2: forever a promise? Current Opinion in Biotechnology, 2020, 62: 48–57
7. Perona-Vico E, Feliu-Paradeda L, Puig S, Bañeras L. Bacteria coated cathodes as an *in-situ* hydrogen evolving platform for microbial electrosynthesis. Scientific Reports, 2020, 10(1): 19852
8. Li H, Opgenorth P H, Wernick D G, Rogers S, Wu T Y, Higashide W, Malati P, Huo Y X, Cho K M, Liao J C. Integrated electromicrobial conversion of CO_2 to higher alcohols. Science, 2012, 335(6076): 1596
9. Krieg T, Sydow A, Faust S, Huth I, Holtmann D. CO_2 to terpenes: autotrophic and electroautotrophic α-humulene production with *Cupriavidus necator*. Angewandte Chemie International Edition, 2018, 57(7): 1879–1882
10. Sakimoto K K, Wong A B, Yang P D. Self-photosensitization of nonphotosynthetic bacteria for solar-to-chemical production. Science, 2016, 351(6268): 74–77
11. Xiu S Y, Yao J N, Wu G M, Huang Y M, Yang B, Huang Y, Lei L C, Li Z J, Hou Y. Hydrogen-mediated electron transfer in hybrid microbial-inorganic systems and application in energy and the environment. Energy Technology (Weinheim), 2019, 7(8): 1800987
12. Liu C, Colón B C, Ziesack M, Silver P A, Nocera D G. Water splitting-biosynthetic system with CO_2 reduction efficiencies exceeding photosynthesis. Science, 2016, 352(6290): 1210–1213
13. Wang M, Zhong W, Zhang S S, Liu R J, Xing J M, Zhang G J.

An overall water-splitting polyoxometalate catalyst for the electromicrobial conversion of CO_2 in neutral water. Journal of Materials Chemistry A, 2018, 6(21): 9915–9921

14. Rodrigues R M, Guan X, Iñiguez J A, Estabrook D A, Chapman J O, Huang S Y, Sletten E M, Liu C. Perfluorocarbon nanoemulsion promotes the delivery of reducing equivalents for electricity-driven microbial CO_2 reduction. Nature Catalysis, 2019, 2(5): 407–414
15. Sakimoto K K, Kornienko N, Cestellos-Blanco S, Lim J, Liu C, Yang P D. Physical biology of the materials—microorganism interface. Journal of the American Chemical Society, 2018, 140(6): 1978–1985
16. Torella J P, Gagliardi C J, Chen J S, Bediako D K, Colón B, Way J C, Silver P A, Nocera D G. Efficient solar-to-fuels production from a hybrid microbial—water-splitting catalyst system. Proceedings of the National Academy of Sciences of the United States of America, 2015, 112(8): 2337–2342
17. Singh N, Savanur M A, Srivastava S, D'Silva P, Mugesh G. A redox modulatory Mn_3O_4 nanozyme with multi-enzyme activity provides efficient cytoprotection to human cells in a Parkinson's disease model. Angewandte Chemie International Edition, 2017, 56(45): 14267–14271
18. Liu Y, Cao X, Ge J. Antioxidative composites based on multienzyme systems encapsulated in metal−organic frameworks. ACS Applied Materials & Interfaces, 2021, 13(39): 46431–46439
19. Abdi Z, Balaghi S E, Sologubenko A S, Willinger M G, Vandichel M, Shen J R, Allakhverdiev S I, Patzke G R, Najafpour M M. Understanding the dynamics of molecular water oxidation catalysts with liquid-phase transmission electron microscopy: the case of Vitamin B_{12}. ACS Sustainable Chemistry & Engineering, 2021, 9(28): 9494–9505
20. Slavin Y N, Asnis J, Häfeli U O, Bach H. Metal nanoparticles: understanding the mechanisms behind antibacterial activity. Journal of Nanobiotechnology, 2017, 15(1): 65
21. Bian B, Bajracharya S, Xu J, Pant D, Saikaly P E. Microbial electrosynthesis from CO_2: challenges, opportunities and perspectives in the context of circular bioeconomy. Bioresource Technology, 2020, 302: 122863
22. Yi J D, Xu R, Chai G L, Zhang T, Zang K T, Nan B, Lin H, Liang Y L, Lv J Q, Luo J, Si R, Huang Y B, Cao R. Cobalt single-atoms anchored on porphyrinic triazine-based frameworks as bifunctional electrocatalysts for oxygen reduction and hydrogen evolution reactions. Journal of Materials Chemistry A, 2019, 7(3): 1252–1259
23. Ayed C, Huang W, Zhang K A. Covalent triazine framework with efficient photocatalytic activity in aqueous and solid media. Frontiers of Chemical Science and Engineering, 2020, 14(3): 397–404
24. Xiang Z H, Xue Y H, Cao D P, Huang L, Chen J F, Dai L M. Highly efficient electrocatalysts for oxygen reduction based on 2D covalent organic polymers complexed with non-precious metals. Angewandte Chemie International Edition, 2014, 53(9): 2433–2437
25. Liu J L, Hu Y J, Cao J J. Covalent triazine-based frameworks as efficient metal-free electrocatalysts for oxygen reduction reaction in alkaline media. Catalysis Communications, 2015, 66: 91–94
26. García Á, Retuerto M, Dominguez C, Pascual L, Ferrer P, Gianolio D, Serrano A, Aßmann P, Sanchez D G, Peña M A, Rojas S. Fe doped porous triazine as efficient electrocatalysts for the oxygen reduction reaction in acid electrolyte. Applied Catalysis B: Environmental, 2020, 264: 118507
27. Zhuo H Y, Zhang X, Liang J X, Yu Q, Xiao H, Li J. Theoretical understandings of graphene-based metal single-atom catalysts: stability and catalytic performance. Chemical Reviews, 2020, 120(21): 12315–12341
28. Feng S H, Zheng W Z, Zhu J K, Li Z J, Yang B, Wen Z H, Lu J G, Lei L C, Wang S B, Hou Y. Porous metal-porphyrin triazine-based frameworks for efficient CO_2 electroreduction. Applied Catalysis B: Environmental, 2020, 270: 118908
29. Alarawi A, Ramalingam V, He J H. Recent advances in emerging single atom confined two-dimensional materials for water splitting applications. Materials Today. Energy, 2019, 11: 1–23
30. Gao C, Low J X, Long R, Kong T T, Zhu J F, Xiong Y J. Heterogeneous single-atom photocatalysts: fundamentals and applications. Chemical Reviews, 2020, 120(21): 12175–12216
31. LaBelle E V, Marshall C W, May H D. Microbiome for the electrosynthesis of chemicals from carbon dioxide. Accounts of Chemical Research, 2020, 53(1): 62–71
32. Zhou R F, Zheng Y, Jaroniec M, Qiao S Z. Determination of the electron transfer number for the oxygen reduction reaction: from theory to experiment. ACS Catalysis, 2016, 6(7): 4720–4728
33. Yao J, Cheng Y, Zhou M, Zhao S, Lin S C, Wang X Y, Wu J J X, Li S R, Wei H. ROS scavenging Mn_3O_4 nanozymes for *in vivo* anti-inflammation. Chemical Science (Cambridge), 2018, 9(11): 2927–2933
34. Chen M, Zhou X F, Chen X Y, Cai Q H, Zeng R J X, Zhou S G. Mechanisms of nitrous oxide emission during photoelectrotrophic denitrification by self-photosensitized *Thiobacillus denitrificans*. Water Research, 2020, 172: 115501
35. Huang J W, Su Y, Zhang Y D, Wu W Q, Wu C Y, Sun Y H, Lu R F, Zou G F, Li Y R, Xiong J. FeO_x/FeP hybrid nanorods neutral hydrogen evolution electrocatalysis: insight into interface. Journal of Materials Chemistry A, 2018, 6(20): 9467–9472
36. Tan Y W, Luo M, Liu P, Cheng C, Han J H, Watanabe K, Chen M W. Three-dimensional nanoporous $Co_9S_4P_4$ pentlandite as a bifunctional electrocatalyst for overall neutral water splitting. ACS Applied Materials & Interfaces, 2019, 11(4): 3880–3888
37. Wang N, Cheng G, Guo L P, Tan B E, Jin S B. Hollow covalent triazine frameworks with variable shell thickness and morphology. Advanced Functional Materials, 2019, 29(43): 1904781
38. Dai K, Hu T P, Zhang J F, Lu L H. Carbon nanotube exfoliated porous reduced graphene oxide/CdS-diethylenetriamine heterojunction for efficient photocatalytic H_2 production. Applied Surface Science, 2020, 512: 144783
39. Zheng Y, Chen S, Song H, Guo H, Zhang K A I, Zhang C, Liu T. Nitrogen-doped hollow carbon nanoflowers from a preformed covalent triazine framework for metal-free bifunctional electrocatalysis. Nanoscale, 2020, 12(27): 14441–14447
40. Lu M, Qian Y J, Yang C C, Huang X, Li H, Xie X J, Huang L, Huang W. Nitrogen-enriched pseudographitic anode derived from silk cocoon with tunable flexibility for microbial fuel cells. Nano

Energy, 2017, 32: 382–388

41. Zhu Y P, Li J J, Chen Y B, Zou J, Cheng Q Q, Chen C, Hu W B, Zou L L, Zou Z Q, Yang B, Yang H. Switching the oxygen reduction reaction pathway via tailoring the electronic structure of FeN_4/C catalysts. ACS Catalysis, 2021, 11(21): 13020–13027
42. Ball B, Chakravarty C, Sarkar P. Silicon and phosphorus Co-doped bipyridine-linked covalent triazine framework as a promising metal-free catalyst for hydrogen evolution reaction: a theoretical investigation. Journal of Physical Chemistry Letters, 2020, 11(4): 1542–1549
43. Pohlmann A, Fricke W F, Reinecke F, Kusian B, Liesegang H, Cramm R, Eitinger T, Ewering C, Pötter M, Schwartz E, Strittmatter A, Voß I, Gottschalk G, Steinbüchel A, Friedrich B, Bowien B. Genome sequence of the bioplastic-producing "Knallgas" bacterium *Ralstonia eutropha* H16. Nature Biotechnology, 2006, 24(10): 1257–1262
44. Fernández-Castro P, Vallejo M, San Román M F, Ortiz I. Insight on the fundamentals of advanced oxidation processes. Role and review of the determination methods of reactive oxygen species. Journal of Chemical Technology and Biotechnology, 2015, 90(5): 796–820
45. Nosaka Y, Nosaka A Y. Generation and detection of reactive oxygen species in photocatalysis. Chemical Reviews, 2017, 117(17): 11302–11336
46. Liu Y, Zhao Y, Wang J L. Fenton/Fenton-like processes with *in-situ* production of hydrogen peroxide/hydroxyl radical for degradation of emerging contaminants: advances and prospects. Journal of Hazardous Materials, 2021, 404: 124191
47. Li Y, Zhang W, Niu J F, Chen Y S. Mechanism of photogenerated reactive oxygen species and correlation with the antibacterial properties of engineered metal-oxide nanoparticles. ACS Nano, 2012, 6(6): 5164–5173
48. Li Y, Huang J H, Hu X, Bi L L, Cai P W, Jia J C, Chai G L, Wei S Q, Dai L M, Wen Z H. Fe vacancies induced surface FeO_6 in nanoarchitectures of N-doped graphene protected β-FeOOH: effective active sites for pH-universal electrocatalytic oxygen reduction. Advanced Functional Materials, 2018, 28(34): 1803330